Scalar Relativistic Computations and Localized Orbital Analyses of Nuclear Hyperfine Coupling and Paramagnetic NMR Chemical Shifts

Fredy Aquino, Ben Pritchard, and Jochen Autschbach*

Department of Chemistry, University at Buffalo, State University of New York, Buffalo, New York 14260–3000

Ⓢ *Supporting Information*

ABSTRACT: A method is reported by which calculated hyperfine coupling constants (HFCCs) and paramagnetic NMR (pNMR) chemical shifts can be analyzed in a chemically intuitive way by decomposition into contributions from localized molecular orbitals (LMOs). A new module for density functional calculations with nonhybrid functionals, global hybrids, and range-separated hybrids, utilizing the two-component relativistic zeroth-order regular approximation (ZORA), has been implemented in the parallel open-source NWChem quantum chemistry package. Benchmark results are reported for a test set of few-atom molecules with light and heavy elements. Finite nucleus effects on ^{199}Hg HFCCs are shown to be on the order of -11 to -15%. A proof of concept for the LMO analysis is provided for the metal and fluorine HFCCs of TiF_3 and NpF_6. Calculated pNMR chemical shifts are reported for the 2-methylphenyl-*t*-butylnitroxide radical and for five cyclopentadienyl (Cp) sandwich complexes with 3d metals. Nickelocene and vanadocene carbon pNMR shifts are analyzed in detail, demonstrating that the large carbon pNMR shifts calculated as $+1540$ for Ni (exptl.: $+1514$) and -443 for V (exptl.: -510) are caused by different spin-polarization mechanisms. For Ni, Cp to Ni π back-donation dominates the result, whereas for vanadocene, V to Cp σ donation with relaxation of the carbon 1s shells can be identified as the dominant mechanism.

1. INTRODUCTION

The isotropic nuclear hyperfine coupling constant (HFCC) A_{iso} and, more generally, the hyperfine coupling (HFC) "tensor" (as it is usually referred to), are of importance in electron paramagnetic resonance (EPR) spectroscopy.[1−3] Further, hyperfine interactions play a crucial role in the NMR of paramagnetic molecules.[4−8] In paramagnetic NMR (pNMR), HFCCs are sometimes associated with large "contact" shifts[5,7,9] arising from the interaction of the electron spin-density with the nuclear spin right at the nucleus of interest. Such contact shifts tend to dominate paramagnetic effects in the NMR spectrum for molecules where the electron spin-density has non-negligible contributions at the nuclei for which NMR parameters are measured, e.g., in organic radicals or for transition metal complexes where an open metal d shell participates in bonding with the ligands. The anisotropic part of the HFC tensor, along with the anisotropic part of the g-shift tensor, gives rise to pNMR pseudo-contact (PC) chemical shifts.[4,5] In simple cases, the PC shifts arise from the through-space dipolar magnetic interaction of a strongly localized electron spin-density with a nuclear spin elsewhere in a molecule.[4,8,10] An example would be the spin-density of an open 4f shell an a lanthanide complex magnetically interacting with a ligand nuclear spin. If the lanthanide 4f shell does not participate in metal ligand bonding, the spin-density is localized at the metal center, and contact shifts can be small relative to the PC shifts. In more general formalisms of pNMR,[5] a distinction between contact and PC shifts can be maintained in the sense that the former are calculated from A_{iso} and the latter from the anisotropic part of the HFC tensor, but no assumption has to be made about spatial localization of the spin-density in order to calculate the PC shifts.[8] Calculations of HFC tensors with density functional theory (DFT) were shown

to be reasonably accurate to aid interpretations of EPR spectra for a variety of compounds with light and heavy elements[6,11,12] and to reproduce pNMR chemical shifts.[5,7−9] The quality of the density functional plays an important role in this context. The reliability of first-principles theoretical methods has reached a level that is of practical use in assisting the assignment of experimental spectra and predicting the outcome of measurements. There is an increasing need for quantitative analysis tools that can be used to extract chemically meaningful information about the reasons for an observed magnitude or sign of a HFC tensor in terms of structure and bonding. Herein, we aim to address the quality of the functional as well as the analysis aspect.

This work reports a new two-component relativistic DFT implementation for HFC tensors in the massively parallel open source NWChem quantum chemistry package. The new module performs linear response computations of HFC tensors within the relativistic zeroth-order regular approximation[13] (ZORA) framework, using "pure" (nonhybrid), regular (global) hybrid, and range-separated hybrid density functionals. Further, an analysis tool for HFC tensors in terms of localized molecular orbitals (LMOs, specifically: localized orbitals obtained from the natural bond orbital (NBO) method by Weinhold[14]) has been developed, allowing the dissection of the calculated results in a chemically intuitive manner. Computations of HFCCs for small molecules are reported in order to verify the method and to study the sensitivity of the coupling constants to approximations in the density functional. A proof-of-concept for the LMO analysis of isotropic HFCCs is provided for two metal complexes, TiF_3 and NpF_6. pNMR proton and ^{13}C

chemical shifts were calculated for a set of metallocenes studied previously by Hrobarik et al.[9] These systems afford large pNMR shifts for the ligand atoms that are dominated by the isotropic HFCCs. LMO analyses of selected coupling constants were performed to rationalize the sign and magnitude of the pNMR chemical shifts. Detailed analyses for nickelocene and vanadocene, which yield pNMR chemical shifts at the extreme positive and negative ends of the 3d metallocene chemical shift range, demonstrate the role of the metal orbitals and of spin-polarization in the ligands. For the Ni complex, donation of β spin-density into formally unoccupied metal d_π orbitals is shown to be the main mechanism that determines the sign and magnitude of the C and H pNMR chemical shifts. The vanadium case is more complicated, yielding contributions of opposite signs. The spatial extension of the $3d_\sigma$ orbitals in the two complexes, and the resulting differing interaction with the cyclopentadienyl ligands, is shown to play an important role. The applicability of the computational protocol for predictions of pNMR shifts and the performance of different functionals is also demonstrated for the organic radical 2-methylphenyl-t-butylnitroxide (MPBN).

Section 2 provides an outline of the theoretical framework and details of the implementation. Section 3 provides additional details about the computations. The results are discussed and analyzed in section 4, beginning with a small-molecule benchmark (section 4.1), followed by a proof of principle for the LMO analysis (section 4.2), an investigation of finite-nucleus effects for mercury hyperfine coupling constants (section 4.3), and concluding with calculations and LMO analyses of pNMR chemical shifts (section 4.4). Concluding remarks can be found in section 5.

2. THEORETICAL METHODS

In this work, spin−orbit (SO) effects are treated as a perturbation. An element u, v of the hyperfine coupling (HFC) tensor with $u,v \in \{x, y, z\}$ can be defined as a second derivative of the molecular energy with respect to the effective electron spin S and the nuclear spin μ_N as[2]

$$A_{uv} = \frac{\partial^2 E}{\partial I_u \partial S_v} = g_N \beta_N \frac{\partial^2 E}{\partial \mu_{N,u} \partial S_v} \tag{1}$$

Here, g_N is the nuclear g-factor for the isotope of interest, and β_N is the nuclear magneton. The derivatives are assumed to be taken at $I_u = 0$ to eliminate higher-order terms from the nuclear spin perturbation. The calculation of HFC based on eq 1 has been newly implemented in the NWChem quantum chemistry package within the ZORA framework to treat relativistic effects and using density functional theory for electron correlation. The implementation employs similar techniques as recently reported for ZORA calculations of HFC tensors and electronic g-shift tensors via the linear response (second derivative) route,[8,10,15] and therefore only a brief outline of the theoretical framework is provided in the following for the convenience of the reader.

The HFC calculations are performed on top of spin-unrestricted scalar (spin-free) ZORA DFT calculations, utilizing α and β spin molecular orbitals (MOs), respectively, which are expressed in an atom-centered Gaussian-type basis set $\{\chi_r\}$ (atomic orbitals, AOs). The MO coefficients are $C_{ri}^{(0)}$ (unperturbed) and $C_{ri}^{(v)}$ (perturbed, by the v component of the nuclear spin magnetic moment or by the v component of the SO operator derivative with respect to the electron spin). Let

$P_{rs}^{(0)\alpha-\beta}$ be an element of the scalar relativistic unperturbed spin-density matrix in the AO basis

$$P_{rs}^{(0)\alpha-\beta} = \sum_i n_i^\alpha C_{ri}^{(0)\alpha} C_{si}^{*(0)\alpha}$$
$$- \sum_i n_i^\beta C_{ri}^{(0)\beta} C_{si}^{*(0)\beta} \tag{2}$$

where n_i^γ indicates the orbital occupation number for orbital i with spin projection γ. Correspondingly, $P_{rs}^{(v)\alpha-\beta}$ is an element of the linear response of $P_{rs}^{\alpha-\beta}$ with respect to the static perturbation v. Let $n_\alpha - n_\beta = \sum_i n_i^\alpha - \sum_i n_i^\beta$, assumed to be nonzero. An element of the HFC tensor is then obtained from the sum of the ZORA Fermi "contact" and spin-dipole (FC +SD) term

$$A_{uv}^{\text{FC+SD}} = \frac{2g_N\beta_N}{n_\alpha - n_\beta} \sum_{r,s} P_{rs}^{(0)\alpha-\beta} h_{sr}^{(u,v)} \tag{3a}$$

which requires only the knowledge of the unperturbed MOs/ the unperturbed density matrix and the linear response paramagnetic spin-orbital (PSO)−spin-orbit (SO) cross term

$$A_{uv}^{\text{PSOSO}} = \frac{2g_N\beta_N}{n_\alpha - n_\beta} \sum_{r,s} P_{rs}^{(v)\alpha-\beta} h_{sr}^{(u)} \tag{3b}$$

which requires to solve a set of coupled-perturbed Kohn−Sham (CPKS) equations with a perturbation AO matrix $h_{rs}^{(v)}$ in order to obtain the perturbed density matrix. We have chosen the SO operator derivative for this step. The implementation allows for the use of a spherical Gaussian nuclear model[16,17] described by an exponent ζ_N (such that $\zeta_N \to \infty$ corresponds to a point nucleus). The operator matrix elements $h_{rs}^{(v)}$, $h_{rs}^{(u)}$, and $h_{rs}^{(u,v)}$ are calculated in the AO basis by numerical integration as follows:

$$h_{rs}^{(u)} = -\frac{i}{2} \int d^3r\, \mathcal{K}P\left(\frac{3}{2}, \tilde{r}_N^2\right)$$
$$(\mathbf{U}_N \times [\chi_r^*(\nabla\chi_s) - (\nabla\chi_r^*)\chi_s])_u \tag{4a}$$

$$h_{rs}^{(v)} = \frac{i}{2} \int d^3r (\mathcal{K} - 1)[\{\nabla\chi_r^*\} \times \{\nabla\chi_s\}]_v \tag{4b}$$

$$h_{rs}^{(u,v)} = -\frac{1}{2}\delta_{uv} \int d^3r\, \mathcal{K}P\left(\frac{3}{2}, \tilde{r}_N^2\right)\mathbf{U}_N \cdot \nabla(\chi_r^*\chi_s)$$
$$+ \frac{1}{2} \int d^3r\, \mathcal{K}P\left(\frac{3}{2}, \tilde{r}_N^2\right)U_{N,v}\nabla_u(\chi_r^*\chi_s) \tag{4c}$$

where $\tilde{\mathbf{r}}_N = (\xi_N)^{1/2}\mathbf{r}_N$ is a scaled electron−nucleus (N) distance and $\mathbf{U}_N = c^{-2}\mathbf{r}_N^{-3}\mathbf{r}_N$. Further, $P(a,x)$ is the lower incomplete γ function ratio $P(a,x) = (1/\Gamma(a)) \int_0^x t^{a-1}e^{-t}\, dt$, and $\mathcal{K}$ is a kinematic factor common in all operators arising from within the ZORA framework:

$$\mathcal{K} = \frac{2c^2}{2c^2 - V} \tag{5}$$

The potential V entering $\mathcal{K}$ is in NWChem approximated by a sum of atomic Hartree potentials.[18,19] For $\mathcal{K} \to 1$ and $\zeta_N \to \infty$, the well-known nonrelativistic point-nucleus versions of the operator matrix elements are obtained.[8]

After the HFC matrix is determined, it is transformed to its principal axis system (PAS). For each principal component, an analysis of the result in terms of localized molecular orbitals

(LMOs) is performed using the natural bond orbital (NBO) methodology as devised by Weinhold.[14] Previous methods for ZORA-based analyses of molecular properties in the NBO framework[19–24] have been extended to accommodate spin-unrestricted DFT calculations. The NBO program uses the ground state density matrix in order to determine a set of strongly localized natural bond spin orbitals (NBOs) Ω_j^γ and a set of "natural" spin LMOs ϕ_j^γ that are related by

$$\phi_j^\gamma = \Omega_j^\gamma W_{jj}^\gamma + \sum_{n \neq j} \Omega_n^\gamma W_{nj}^\gamma = \sum_r \chi_r D_{rj}^\gamma \tag{6}$$

where $\gamma = \alpha$ or β spin. D_{rj}^γ represents the LMO coefficients in the AO basis. The $n = j$ term in eq 6 is a localized "parent NBO" of a more or less strongly localized LMO, which may be considered as the "localized" (L) part of the LMO. In the NBO literature, this term is often referred to as the "Lewis" part[14,25] because it tends to correspond to an electron in a molecule's Lewis formula. The remaining component ($n \neq j$) is the nonlocalized (NL, delocalization, "non-Lewis") tail of the LMO. For systems where delocalization is important, the NL tails of the LMOs can be substantial. The NBOs are expressed in the AO basis as

$$\Omega_n^\gamma = \sum_r \chi_r B_{rn}^\gamma \tag{7}$$

The analysis of a response property in a basis of LMOs is facilitated by the orthogonal LMO-to-MO transformation T:

$$C_{ri}^\gamma = \sum_j D_{rj}^\gamma T_{ji}^\gamma \; ; \; T_{ji}^\gamma = \sum_{r,s} D_{rj}^{\gamma *} S_{rs} C_{si}^\gamma \tag{8}$$

which is readily obtained from the MO and LMO coefficients in the AO basis and the elements S_{rs} of the overlap matrix of the AO basis if it is not explicitly available. Further,

$$C_{ri}^\gamma = \sum_{n,j} B_{rn}^\gamma W_{nj}^\gamma T_{ji}^\gamma \tag{9}$$

Since the analysis determined individual orbital contributions to the HFC tensor elements, it is convenient to introduce a matrix $U_{ai}^{(m)}$ such that $C_{ri}^{(m)} = \sum_a C_{ra} U_{ai}^{(m)}$ for each spin gives the perturbed canonical MO coefficients from the CPKS procedure for the perturbation in the direction of one of the principal components $m = 1-3$ of the hyperfine tensor. The operator matrices are also transformed to the PAS. Equation 9 is substituted for one set of unperturbed MO coefficients in each term entering the density matrix and its perturbation in eq 3. The NBO/NLMO decomposition of the tensor component is in this way obtained for each spin $\gamma = \alpha, \beta$ as

$$A_{mm}^\gamma = 2Re \overset{\text{LMO}}{\sum_j} \overset{\text{NBO}}{\sum_n} \overset{\text{MO}}{\sum_i} \overset{\text{basis}}{\sum_{r,s}} \{ n_i^\gamma [h_{rs}^{\text{PSO},(m)}$$
$$\overset{\text{MO}}{\sum_a} C_{sa}^\gamma U_{ai}^{SO,\gamma(m)}] + h_{rs}^{\text{FC+SD},(mm)} C_{si}^\gamma \}$$
$$[B_{rn}^\gamma W_{nj}^\gamma T_{ji}^\gamma]^{\gamma *} \tag{10}$$

where the FC+SD and PSOSO terms have been added to obtain a compact formulation. The analysis program has been written in such a way that the FC+SD and PSOSO contributions can also be analyzed separately for each principal component. In this work, we report analysis results for the isotropic hyperfine coupling, $A_{\text{iso}} = (1/3)\sum_{m=1}^3 (A_{mm}^\alpha - A_{mm}^\beta)$.

The NBO-LMO specific contributions in eq 10 are the B, W, and T terms. If an analysis is carried out with other sets of localized orbitals (e.g., obtained from the Boys[26] or from the Pipek–Mezey[27] criteria), there is typically an orthogonal matrix T or the localized MO coefficients in the basis, or both, available. Equation 10 is in this case also applicable if one omits the NBO related terms; i.e., $B_{rn} W_{nj}$ is replaced by $D_{rn}\delta_{nj}$ for each spin. Skipping the MO localization altogether corresponds to an analysis in terms of canonical MOs, which means $B_{rn}\delta_{nj}$ is replaced by $C_{rn}\delta_{nj}\delta_{ji}$. Equation 10 can be split into individual contributions in different ways. In this work, we only report results from full summations over n, i, r, and s without a separate breakdown into $j = n$ terms (L) and the remainder $j \neq n$ (NL). An alternative way to study contributions to the HFC would be to carry out the sums j, i, r, and s and provide a breakdown per NBO.

The formalism outlined here corresponds to "unscaled" ZORA computations. A "scaled" ZORA variant has been suggested by Wolff et al.[28] for calculations of NMR shielding tensors, and it was recently also used by us in ZORA calculations of g-shifts.[15] One may adopt a similar approach for HFC. In the scalar relativistic ZORA framework, scaling factors for each canonical spin-orbital φ_i^γ are calculated as

$$S_i^\gamma = \left[1 + \langle \varphi_i^\gamma | \hat{\mathbf{p}} \frac{c^2}{[2c^2 - V]^2} \hat{\mathbf{p}} | \varphi_i^\gamma \rangle \right]^{-1} \tag{11}$$

The scaling factors are then included in the unperturbed and perturbed density matrices in the summation over i (see eq 2[19]). In the LMO analysis code, if an option for ZORA scaling is set, the unperturbed MO coefficients are scaled by $(S_i^\gamma)^{1/2}$ at the beginning. The implementation uses the right-hand side of eq 8 to obtain the matrix T, resulting in columns scaled by $(S_i^\gamma)^{1/2}$. The combination of scaled C and T matrices in eq 10 then gives the scaled-ZORA result from the LMO analysis.

3. COMPUTATIONAL DETAILS

The calculations were carried out with a locally modified 2011 developer's version of the open source NWChem package.[29–31] Recently implemented ZORA functionality reported by Nichols et al.[18] and by us[15,19] has been further developed to enable scalar ZORA linear response DFT computations of HFC tensors as described in section 2. In addition, a recently developed ZORA code for NMR shielding in NWChem[15] has been modified to accommodate spin-unrestricted calculations to obtain the "orbital" shifts of section 4.4. Computations of g-tensors, also needed for pNMR chemical shifts, were performed with a corresponding ZORA module that was recently developed in NWChem.[15] Consistent with previous ZORA implementations of g-shifts and hyperfine coupling as second order derivatives,[8,10,15] spin - other-orbit (SOO) terms have been omitted. For a justification of this approximation, see ref 32. For the small molecule benchmark (section 4.1), fully uncontracted ANO-RCC basis sets[33] were used for metal atoms (Ti, Hg, Np). The highest angular momentum basis functions (h for Np and Ti and g for Hg) have been removed from the ANO basis sets since previous work on electric field gradients and g-shift tensors indicated that DFT calculations at the level performed here do not benefit much from these functions.[15,19] For light atoms, the pcJ4 basis by Jensen[34,35] was used. This basis has been designed for J-coupling and should therefore also

Table 1. HFCC Calculated with NWChem Using the Non-Hybrid PBE Functional, the Global Hybrid PBE0, and the Range-Separated CAM-B3LYP Hybrid (CAM)[a]

molecule	atom	PBE			PBE0			CAM			exptl
		FC+SD	PSOSO	total	FC+SD	PSOSO	total	FC+SD	PSOSO	total	
CH_2	C	211.2	−0.2728	210.9	225.5	−0.2691	225.2	219.1	−0.2792	218.8	
CH_2	H	−18.72	0.0080	−18.71	−24.62	0.0078	−24.61	−14.42	0.0081	−14.41	
CH_3	C	70.80	−0.2470	70.56	84.90	−0.2495	84.65	76.29	−0.2574	76.04	108[b]
CH_3	H	−64.43	0.0159	−64.42	−72.75	0.0151	−72.74	−65.76	0.0158	−65.74	−64.46[b]
CHO	C	379.0	−0.5174	378.5	387.7	−0.5369	387.1	390.1	−0.5676	389.5	365[c]
CHO	H	371.6	−0.0773	371.5	374.8	−0.0791	374.8	394.8	−0.0810	394.7	354[c]
CHO	O	−24.45	0.5841	−23.86	−34.27	0.5628	−33.71	−35.23	0.5710	−34.66	
HSiO	Si	−531.7	1.125	−530.5	−547.0	1.0999	−545.9	−588.7	1.124	−587.6	−630[d]
HSiO	H	428.6	−0.0261	428.6	432.4	−0.0265	432.4	477.1	−0.0276	477.1	450[d]
HSiO	O	−6.805	0.2069	−6.598	−11.11	0.1569	−10.96	−11.14	0.1169	−11.03	
HSiS	Si	−496.5	1.923	−494.5	−507.5	1.9906	−505.5	−522.5	2.162	−520.4	
HSiS	H	327.3	−0.0641	327.3	328.4	−0.0667	328.4	356.3	−0.0717	356.2	
HSiS	S	0.4938	−0.1963	0.2975	1.380	−0.0662	1.314	−1.435	0.2176	−1.218	
SiOH	O	−21.45	0.6915	−20.76	−21.26	0.6995	−20.56	−21.17	0.9825	−20.19	
SiOH	Si	33.50	7.003	40.50	19.25	7.388	26.63	12.65	10.36	23.01	
SiOH	H	54.39	−0.1406	54.25	51.57	−0.1371	51.44	52.53	−0.1834	52.35	
SiSH	S	24.15	−0.1318	24.02	19.99	−0.1238	19.87	21.28	−0.1427	21.13	
SiSH	Si	30.53	5.214	35.74	14.82	5.507	20.33	9.180	6.946	16.13	
SiSH	H	129.0	−0.0595	128.9	120.4	−0.0577	120.3	122.3	−0.0640	122.3	
HgH	Hg	6812	−200.6	6612	7243	−202.2	7041	7375	−206.9	7168	7002[e]
HgH	H	747.2	−1.864	745.3	728.3	−1.700	726.6	771.7	−1.724	770.0	710[e]
HgF	Hg	17744	−21.25	17722	19016	−34.31	18982	19902	−28.64	19873	22163[f]
HgF	F	239.5	−149.0	90.47	284.9	−107.8	177.0	271.1	−103.3	167.8	670[f]
TiF_3	Ti	−231.4	2.283	−229.1	−198.5	3.051	−195.5	−203.5	3.253	−200.2	184.8[g]
TiF_3	F	2.694	0.7281	3.422	−15.42	0.7866	−14.63	−10.22	0.9564	−9.265	−23.6[g]
NpF_6	Np	−479.7	−1631	−2111	−206.2	−2138	−2344	−215.0	−2104	−2319	−1994[h]
NpF_6	F	−26.36	−1.493	−27.85	−41.93	−19.94	−61.87	−38.22	−14.88	−53.10	−72.67[h]

[a]Scaled scalar ZORA, Gaussian nucleus model. pcJ4 basis for all atoms with the exception of Hg, Ti and Np where we used an uncontracted ANO basis set, and F in NpF_6 (IGLO-III). [b]Ref 48. [c]Ref 49. [d]Ref 50. Sign was not reported and changed by us to match the sign of the calculated HFCC. [e]Ref 51. [f]Ref 52. [g]Ref 53. [h]Ref 54.

be suitable for HFC computations. Additional sets of scaled and unscaled ZORA computations with other basis sets and various functionals were performed to confirm that the calculated results reported herein are not strongly affected by basis set incompleteness. To verify the new implementation, calculations were performed with the Amsterdam Density Functional (ADF) package[36] for comparison, using a compatible ZORA implementation for HFC tensors[8] but Slater-type instead of Gaussian-type basis sets. The ADF calculations utilized the flexible QZ4P basis.[37]

To investigate finite-nucleus effects (section 4.3), computations on selected Hg containing radicals were carried out with fully uncontracted basis sets designed by Hirao et al.[38,39] for relativistic computations, which were augmented with polarization functions as detailed in ref 40. LMO analyses of the metal and fluorine HFCCs of TiF_3 and NpF_6 (section 4.2) were carried out with the IGLO-III basis[41] for F, which yielded good agreement with benchmark data obtained with the larger pcJ4 basis (see Supporting Information). Accordingly, the computations on metallocenes (section 4.4) were performed with a combination of uncontracted ANO basis sets for the metal, with angular momentum functions of $l > 3$ removed, and the computationally more efficient IGLO-III basis for ligand atoms. Calculations of the MPBN radical also utilized the IGLO-III basis. Zero-field splitting has been neglected in the calculations of pNMR chemical shifts for the metallocenes since it was shown to give rise to only small changes (less than 1 ppm).[9]

Hyperfine data reported in this work are for the following nuclear isotopes (g_N in parentheses): ^1H (5.5857), ^{17}O (−0.7575), ^{19}F (5.2577), ^{29}Si (−1.1106), ^{33}S (0.4292), ^{47}Ti (−0.3154), ^{199}Hg (1.0118), and ^{237}Np (1.256).

Localizations of scalar ZORA spin-orbitals were performed with the NBO 5.0 program.[42] Calculated HFCCs have been analyzed in terms of contributions from individual α and β spin LMOs. The NWChem interface for the analysis program, originally developed for electric field gradients,[19] has been extended to provide the necessary input data for each principal component of the calculated hyperfine tensors. The LMOs were characterized on the basis of data provided by the NBO program, as well as visually by generating isosurface plots. The orbital graphics were generated with the ADF graphical interface using LMO cube data files created by NWChem.

The following density functionals have been used for the calculations (main article and Supporting Information): a combination of the Becke88[43]+Perdew86[44] functionals (BP or BP86), the popular B3LYP functional,[45] the 50% global hybrid BHLYP,[46] a hybrid version (PBE0) of the Perdew−Burke−Ernzerhof (PBE) functional,[44] and the default parametrization of the range-separated hybrid functional CAM-B3LYP (or short: CAM),[47] which affords 19% Hartree−Fock (HF) exchange at very short interelectronic distances and 65% asymptotically. The geometries for the small molecule test set are the same as previously used in refs 8, 10, and 15. These are geometries optimized with the ADF program using spin-

unrestricted scalar ZORA, the BP functional, and the TZ2P Slater-type all-electron basis from the ADF basis set library.[36] For consistency, the metallocenes and the organic radical MPBN were optimized at the same level of theory. For MPBN, an alternative geometry obtained with the B3LYP functional has been employed as well.

4. RESULTS AND DISCUSSION

4.1. Small Molecule Benchmarks. Tables 1 and 2 provide calculated HFCCs for a test set of small molecules. The

Table 2. Comparison of HFCCs Calculated with NWChem (see section 2) and a Recent ZORA Implementation in ADF[8a]

molecule	atom	NW[b]		ADF[c]	
		FC+SD	PSOSO	FC+SD	PSOSO
CH_2	C	225.4	−0.2691	220.9	−0.2450
CH_2	H	−24.62	0.0078	−24.84	0.0080
CH_3	C	84.80	−0.2495	80.12	−0.2210
CH_3	H	−72.75	0.0151	−72.93	0.0160
CHO	C	387.6	−0.5369	381.3	−0.5480
CHO	H	374.9	−0.0791	371.3	−0.0850
CHO	O	−34.21	0.5628	−33.05	0.5220
HSiO	Si	−547.0	1.100	−541.1	1.034
HSiO	H	432.5	−0.0265	437.5	−0.0270
HSiO	O	−11.06	0.1569	−9.588	0.0930
HSiS	Si	−507.5	1.991	−502.9	1.923
HSiS	H	328.5	−0.0667	333.0	−0.0670
HSiS	S	1.305	−0.0660	0.4460	0.0090
SiOH	O	−21.25	0.6995	−20.68	0.7110
SiOH	Si	19.44	7.388	22.18	7.378
SiOH	H	51.57	−0.1371	50.30	−0.1420
SiSH	S	20.00	−0.1238	20.05	−0.1380
SiSH	Si	15.03	5.507	22.77	5.408
SiSH	H	120.4	−0.0577	121.0	−0.0600
HgH	Hg	7247	−200.8	6961	−200.4
HgH	H	728.3	−1.6987	734.8	−1.700
HgF	Hg	19033	−33.86	18295	−34.77
HgF	F	284.0	−107.8	273.5	−104.6
TiF_3	Ti	−198.5	3.051	−192.7	3.323
TiF_3	F	−15.41	0.7867	−15.47	0.7640
NpF_6	Np	−232.4	−2105	−200.7	−2804
NpF_6	F	−38.01	−14.88	−44.04	−33.80

[a]PBE0 functional, unscaled ZORA, Gaussian nucleus model. [b]pcJ4 basis for all atoms except Hg, Ti, and Np where an uncontracted ANO basis set was used. Also, for NpF_6, we used IGLO-III for fluorine. [c]QZ4P basis set for all atoms.

calculations were performed with a Gaussian finite nucleus model as detailed in section 2. Table 1 provides HFCCs calculated with the new NWChem implementation with three different density functionals. The results are based on scaled-ZORA calculations, as discussed at the end of section 2. Available experimental data are also provided. Results of additional calculations with unscaled ZORA, and of scaled and unscaled ZORA calculations with point-nuclei, can be found in the Supporting Information (SI). We decided to provide the FC+SD and PSOSO terms separately, usually with four to five significant figures, since they have very different magnitudes for the lighter atomic cases.

The HFCCs show overall moderate, in some cases large, variations upon inclusion of HF exchange into the functional

(going from PBE to one of the hybrids). As an example, the fluorine HFCs in TiF_3, HgF, and NpF_6 are sensitive to the functional and improve when going from PBE to PBE0. The poor agreement of calculations and experimental results for the fluorine HFCC in HgF has been noted previously for ADF calculations with PBE and PBE0;[8] CAM-B3LYP performs similarly to PBE0 in this case. The magnitudes of the fluorine HFCCs calculated with CAM are somewhat lower than with PBE0, which worsens the agreement with experimental results. Similar trends are also seen for other nuclei in several other light atomic systems. The HFCCs for Hg are larger when calculated with the CAM functional compared to PBE0, which improves the agreement with experimental results (most of our calculations underestimate the mercury HFCCs; for further details see section 4.3). Given the relatively small number of experimental data available for comparison, the two hybrid functionals perform about equally well and offer some improvements over PBE. The range-separated functional CAM-B3LYP does not give spectacularly better HFCCs than PBE0, and in some cases (e.g., F in TiF_3 and NpF_6), they do not agree as well with experimental results as their PBE0 counterparts. For the applications reported in the following sections, we therefore decided to use the PBE0 global hybrid functional.

It is interesting to make a direct comparison with ZORA hyperfine couplings calculated with the ADF implementation for the following reason: Apart from differences such as the numerical integration grid, there are some major conceptual differences between the implementations at the hybrid DFT level, namely (i) Gaussian-type basis functions in NWChem vs Slater-type functions in ADF, (ii) approximating V in the ZORA function $\mathcal{K}$ of eq 5 by a sum of atomic Hartree potentials in NWChem vs a sum of atomic local XC potentials in ADF, (iii) approximation of the two-electron integrals in ADF by using density-fitting techniques (vs no formal approximations in NWChem). The different approximations for $\mathcal{K}$ have been investigated recently in ref 15 in the context of g-shift and NMR shielding calculations and were shown to produce very similar results except for the small diamagnetic g-shift of HSiS. A side-by-side comparison of the small-molecule benchmark in Table 2 shows that, despite the methodological differences between the implementations, the calculated HFCCs and the individual FC+SD and PSOSO contributions are for the most part in excellent agreement. Large absolute differences are found for NpF_6 which echo those reported recently for molecular g-tensors.[15] In ref 15, we have analyzed the calculated g-tensors for this molecule in some detail. The most likely cause for the discrepancies is the limitation of the ADF auxiliary basis set to angular momenta of $l \leq 4$. Most of the other differences in the HFCCs calculated with the two codes are in the few-percent range and can be attributed to differences in the basis sets, the integration grid accuracy, and residual errors from the incomplete auxiliary basis in the ADF calculations. Somewhat larger relative deviations are found in some cases where the calculated numbers are small. We also note that the QZ4P basis for lighter atoms is less optimal for HFC calculations than pcJ4 in terms of augmentation with high-exponent basis functions.

The data of Table 2 are based on unscaled ZORA (see section 2). This allows a comparison with the PBE0 column of Table 1 in order to assess the impact from the ZORA scaling. As one might have expected from the expression for the scaling factors, eq 11, the scaling has practically no effect on the

602

dx.doi.org/10.1021/ct2008507 | J. Chem. TheoryComput. 2012, 8, 598−609

HFCCs calculated for molecules with only light elements. The scaling becomes somewhat noticeable for the Hg radicals, and significant for NpF_6, where it appears to be improving the fluorine HFCC toward experiment. Since the experimental value is derived from solid state measurements, perfect agreement with any type of gas phase calculation must not be expected. Theoretical data for the NpF_6 molecule based on Dirac scattered-wave calculations have been reported by Case,[55] who obtained HFCCs of −2020 MHz for Np and −63 MHz for F, in reasonable agreement with the predictions from ZORA DFT.

4.2. LMO Analysis for TiF$_3$ and NpF$_6$. For a first test of the LMO analysis, TiF_3 and NpF_6 were selected. A breakdown of the calculated isotropic hyperfine coupling constants into contributions from different LMO types is provided in Tables 3

Table 3. Localized Molecular Orbital (LMO) Decomposition of the Isotropic Metal Hyperfine Coupling Constant in TiF$_3$ and NpF$_6$ (MHz)

LMO type	TiF$_3$	NpF$_6$
metal core	−44.5	−545.4
F core	0.0	0.3
$\sum \sigma$(Np−F)	−38.9	251.1
metal SOMO	−110.3	−1937.2
$\sum$ all LP	−0.8	−137.3
$\sum$ analysis	−194.5	−2368.4
total calcd.	−194.5	−2368.4

Table 4. Localized Molecular Orbital (LMO) Decomposition of the Isotropic F Hyperfine Coupling Constant in TiF$_3$ and NpF$_6$ (MHz)[a]

LMO type	TiF$_3$	NpF$_6$
metal core	−3.5	−11.5
F* core	−0.6	−4.7
σ(Np−F*)	−142.5	−325.9
F* LP$_\sigma$	126.5	282.1
F* LP$_\sigma$ + σ(Np−F*)	−16.0	−43.8
metal SOMO	6.7	−1.2
$\sum$ other LP and bonds	−0.2	−0.6
$\sum$ analysis	−13.6	−61.7
total calcd.	−13.6	−61.7

[a]F* = atom for which HFCC was calculated.

(metal HFCCs) and 4 (fluorine HFCCs). The computations were performed with the PBE0 hybrid functional, point nuclei, unscaled ZORA, and the IGLO-III basis for F. For further details, see section 3. Comparison with a matching set of calculations with the pcJ4 basis for F (Table S2 in the Supporting Information) shows that the results agree well; the largest relative change is a 1 MHz decrease of the fluorine HFCC magnitude in TiF_3. Formally nonbonding d or f orbitals representing the singly occupied MO (SOMO) are indicated. Metal−ligand σ-bonding LMOs are indicated by σ. Contributions from equivalent orbitals were added. The Weinhold localization produces lone pair LMOs of local σ and π symmetry for halide atoms. The σ lone pairs of fluorine, which play an important role in the ligand HFCCs, are labeled as LP$_\sigma$. For the analysis, contributions from equivalent α and β spin

orbitals have been combined (except, of course, for the SOMO).

The HFCC of Ti in TiF_3 has a simple LMO decomposition: more than half of the total HFCC is generated directly by the spin-density contribution from the SOMO. The magnetic moment of ^{47}Ti is negative, which causes the calculated HFCC to be negative. The localized SOMO, formally being a metal $3d_{z^2}$ orbital, is a 3d−4s hybrid with 12% s character, causing a large hyperfine coupling mainly from the ZORA analog of the FC mechanism. A sizable contribution to the Ti HFCC stems from the Ti core and semicore orbitals, mainly from 2s and 3s. These orbitals contribute with opposite signs to the HFCC; the nonvanishing sum of α and β orbital pairs is attributable to spin-polarization in these shells and to core−core and core−valence orthogonalization. The contributions from individual α and β core orbitals to the Ti HFCC are huge but cancel to a large degree. For instance, the Ti 1s spin−orbitals contribute −847640.7 and +847635.4 MHz, respectively, leaving a modest −5.4 MHz when added. The Ti−F bonding orbitals contribute a combined −39 MHz to the Ti HFCC, indicating that part of the spin-density in the molecule is attributable to these mainly ionic but partially covalent bonds. The NBO algorithms did in fact not autodetect the Ti−F bonds, but they are manifest in low occupancy (0.9) fluorine "lone pairs" with about 10% mixing of Ti orbitals. A sizable s character (24%) of the hybrids on Ti in these Ti−F bonds explains their sizable contributions to the Ti HFCC.

Further, the s/d mixing on Ti and the "spillage" of spin-density into the covalent part of the Ti−F bonds is responsible for the fluorine HFCC in TiF_3. See Table 4 for the LMO data. The magnetic moment of ^{19}F is positive, which means that the negative HFCC is the result of spin-polarization in the system. The direct contribution from the SOMO, an α spin-orbital, is positive as expected. But this term is overpowered by a large negative HFCC from the sum of the σ(Ti−F) α (positive contribution) and β (negative contribution) spin orbitals. Spin-polarization for the fluorine σ lone pair spin orbitals has a strongly balancing effect to that of the Ti−F bonds. There is also a small, but not negligible, negative contribution from the Ti semicore shells to the fluorine HFCC.

The analyses of the Np and F HFCCs in NpF_6 yield qualitatively similar results to those performed for TiF_3 in terms of the relative importance of bond, lone pair, core orbitals, and the SOMO, despite the fact that—unlike in TiF_3—the PSOSO linear response cross term dominates the HFCC for Np and plays a significant role for fluorine. As in TiF_3, the negative fluorine HFCC is the result of spin-polarization in the Np−F bonding LMOs and the F σ lone-pair LMOs, with a strong cancellation between the bond and lone pair LMOs. The Np magnetic moment is positive, but the HFCC is negative. Even though the calculation employs pure α and β spin-orbitals, the effects from SO coupling are evident in the large negative PSOSO perturbation term for the Np hyperfine coupling. The Np−F bonds are significantly more covalent in NpF_6 (16% Np) than in TiF_3 and in the NBO calculation identified as bonding orbitals instead of fluorine lone pairs. The SOMO is essentially a Np $5f_{xyz}$ orbital.

In summary, the LMO analyses for the two molecules provide chemically intuitive answers regarding the origin of the metal and ligand HFCCs. The role of spin-polarization becomes readily evident in an incomplete cancellation of contributions from formally equivalent occupied α and β spin

LMOs, such as the metal−ligand σ bonding LMOs or some of the fluorine lone pair orbitals.

4.3. Finite Nucleus Effects. Finite nucleus effects on HFCCs (and also on NMR J-coupling) can be significant for elements as heavy as Hg[8,17,40] or Np. Table 5 collects mercury

Table 5. Mercury HFCCs Calculated with a Hybrid DFT Formalism and with a Point Nucleus Model (PN) and a Finite Gaussian Nucleus Model (FN)[a]

| molecule	method	NW[b]		ADF[c]	ref[d]
		A_{iso}			
		PBE0	CAM	PBE0	B3PW91
HgH	NR	4084	4210		4470
	PN	7790	7919	7456	9896
	FN	6767	6880	6688	8531
	PN-FN	1023	1039	768	1365
	exptl.	7002	7002		
HgF	NR	8931	9173		9334
	PN	21001	21934	21027	25102
	FN	18335	19154	18956	21490
	PN-FN	2667	2780	2070	3612
	exptl.	22127	22127		
HgCN	NR	7590	7795		7303
	PN	18382	19003	18365	19570
	FN	16000	16543	16721	16430
	PN-FN	2382	2459	1643	3140
	exptl.	15850	15850		
HgAg	NR	2108	2068		2013
	PN	3521	3450	3550	4165
	FN	3154	3109	3201	3456
	PN-FN	367	341	348	709
	exptl.	2723	2723		

[a]Comparison with published DKH2 data ("ref" column) and with nonrelativistic point-nucleus data (NR). [b]Unscaled scalar ZORA with uncontracted Gaussian basis designed for point nuclei used for NR and PN calculations. Finite nucleus Hirao basis set for FN calculations. See section 3. [c]Unscaled scalar ZORA with modified TZ2P Hg basis set from ref 17. See text for details. [d]Scalar relativistic DKH2 data from Malkin et al., ref 40.

HFCCs calculated for HgH, HgF, HgCN, and HgAg, with hybrid density functionals. The reference literature data were taken from Malkin et al.,[40] which are based on scalar relativistic second-order Douglas−Kroll−Hess (DKH2) calculations. A similar table, but with results from nonhybrid functionals, can be found in the Supporting Information. Given the nearly singular nature of the operator in the hyperfine coupling FC matrix elements, eq 4c, which in the nonrelativistic point-nucleus case equals to a δ-function, it is difficult to converge relativistic point nucleus HFC calculations with respect to the basis set. The finite nucleus corrections listed in Table 5 should therefore be considered as estimates for their magnitude, with the more important goal being to obtain well converged finite-nucleus results. For a fair comparison of finite nucleus (FN) versus point nucleus (PN) data, we have adopted corresponding Gaussian-type basis sets optimized for finite nuclei by Nakajima and Hirao[38] and for point nuclei by Tsuchiya et al.,[39] uncontracted, and further augmented as described in ref 40. For comparisons with ADF, a Slater-type basis for Hg augmented with high exponent s and p functions has been taken from ref 17 (basis "TZ2P3" from the cited article, with a highest exponent of 4×10^4). The latter basis set is not expected to

furnish fully converged FC terms, but going beyond this augmentation caused numerical problems in the ADF hyperfine computations. The highest Gaussian exponent in the point nucleus Hirao basis for Hg is 2×10^{11}, much exceeding the square of the highest Slater exponent in the ADF basis, and thus one should expect better converged point nucleus data in the NWChem ZORA computations, along with somewhat larger finite nucleus effects. To illustrate the rather spectacular magnitude of relativistic effects, overall, on the calculated HFCCs, Table 5 also lists nonrelativistic (NR) data obtained with point nuclei.

Inspection of the ZORA results obtained with the NWChem and the ADF implementations demonstrates that, as expected, the finite nucleus corrections (PN-FN) calculated with NWChem and the Hirao basis sets are somewhat larger than those calculated with ADF and the augmented basis set from ref 17. The relativistic "corrections" to the HFCCs of HgF and HgCN are almost a factor of 2 larger than the nonrelativistic PN data. The resulting ratio close to 3 of relativistic to NR hyperfine coupling constants is of the same magnitude as a relativistic scaling factor of the hyperfine integrals calculated for the 6s orbital of the Hg atom,[56−58] indicating that for these molecules the contributions from the Hg 6s orbital dominates the results. The ratio PN/FN of the Hg HFCCs for these molecules is 1.15 (NWChem, PBE0). These ratios slightly exceed the PN/FN ratio of 1.13 calculated for the 6s hyperfine integral from fully numerical atomic DFT calculations ($X\alpha$ functional) for Hg reported in ref 17. The overestimation of the ratio may indicate that the FN Hirao basis results are too small in magnitude and could benefit from a few additional high-exponent basis functions to better converge the FC term. This assessment is corroborated by a comparison of the Hg hyperfine couplings of HgH and HgF with the finite-nucleus data from Table 1; the latter are somewhat larger in magnitude. For the other two molecules, the HFCCs are significantly smaller in magnitude and the trends are not as clear. The finite-nucleus corrections are 12 and 15% for HgAg and HgH, respectively, which is in the same range as those for HgF and HgCN as well as for the Hg atom. The ADF finite-nucleus corrections are between 11 and 13%. The DKH2 data from ref 40 are overall larger in magnitude than the PBE0 results obtained with our new implementation, both for FN and PN, giving better agreement with experimental results than our PBE0 data in some cases and worse in others. The calculated DKH2 finite-nucleus effects are in some cases significantly above the 13% obtained from numerical atomic ZORA and four-component calculations[17] (e.g., 19% for HgCN). One of the reasons for the differences between the present ZORA data and the DKH2 results from the literature might be the different performance of the two approximate relativistic methods for core and semicore shells, but the calculations also differ in many other respects. Recent 4-component results are lower in magnitude, with smaller finite-nucleus effects, than the DKH2 data of Table 5.[69] In terms of agreement with experimental results for the present FN ZORA calculations, switching from PBE0 to CAM offers slight improvements for three of the four Hg radicals, with HgCN being the exception.

4.4. Calculation and Analysis of Paramagnetic NMR Chemical Shifts. pNMR chemical shift tensors can be obtained from the following expression for the pNMR nuclear magnetic shielding tensor for a particular electronic state:[5,8,9]
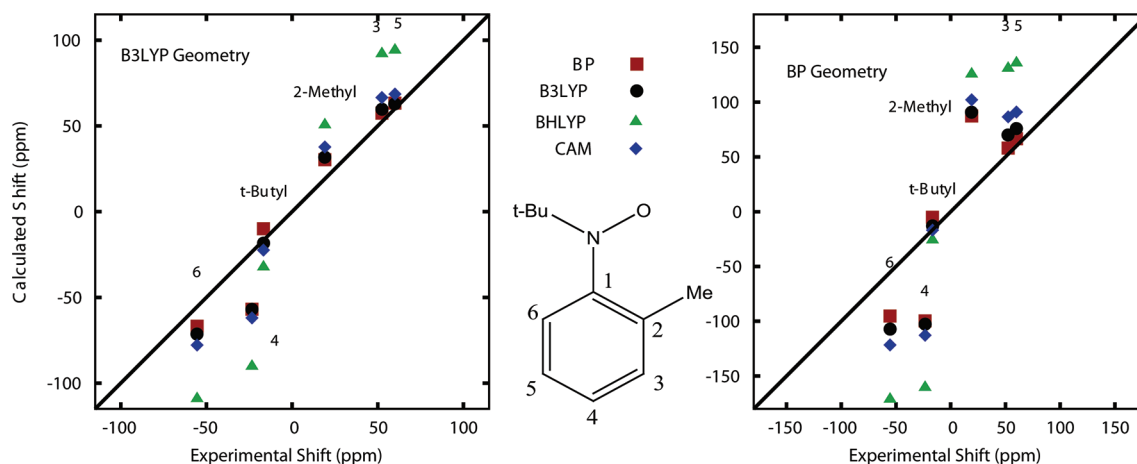
Figure 1. pNMR ^{1}H chemical shifts for MPBN (reference: TMS), calculated with two different geometries and different functionals. Labels in the plots refer to hydrogens bound to the carbons as labeled in the chemical formula.
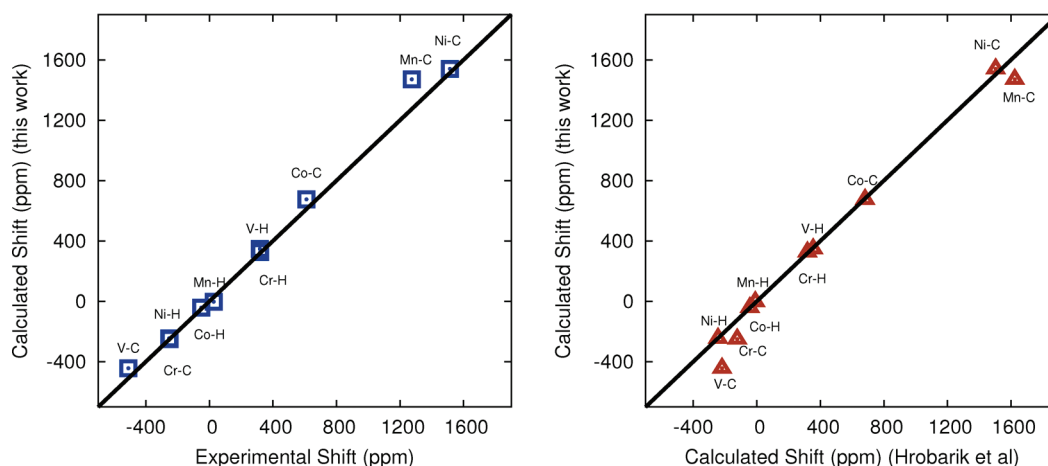
Figure 2. pNMR ^{13}C and ^{1}H ligand chemical shifts with respect to TMS for cyclopentadienyl sandwich complexes with 3d metals. Left: NWChem calculations from this work versus experimental results.[9,59−65] Right: Comparison of present calculations (scaled ZORA, PBE0 functional) with literature data (Hrobarik et al., B3LYP functional[9]). Spin multiplicities are 4 (V), 3 (Cr), 6 (Mn), 2 (Co), and 3 (Ni).

$$\sigma = \sigma^{\text{orb}} - \frac{\beta_e}{g_N \beta_N} \frac{S(S+1)}{3kT} \mathbb{g}\mathbb{A}^T \qquad (12)$$

Here, σ^{orb} is the usual nuclear magnetic shielding tensor calculated as for a diamagnetic system, but with spin-unrestricted orbitals. The electron paramagnetism related terms are contained in the product of the g-tensor ($\mathbb{g}$) and the hyperfine tensor ($\mathbb{A}$); the superscript T indicates a matrix transpose. The shielding constant σ is, as usual, given by the isotropic average of the shielding tensor $\sigma = (1/3)Tr[\sigma]$. Contact shifts may be associated with the isotropic part of $\mathbb{A}$, and PC shifts with its anisotropic part as it contributes to the isotropic average of $\mathbb{g}\mathbb{A}^T$. The calculations reported here are for $T = 298$ K except for manganocene ($T = 389$ K).

As pointed out in the Introduction, HFCCs are vital for the theoretical prediction of pNMR chemical shifts. The 2-methylphenyl-t-butylnitroxide (MPBN) radical has been among the first test cases demonstrating the usefulness of DFT calculations to predict pNMR chemical shifts for organic radicals by eq 12.[5] Figure 1 displays calculated pNMR shifts versus experimental results. The data for the BP functional and the B3LYP optimized geometry agree well with those reported previously by Moon and Patchkovskii.[5] pNMR shifts calculated

with the global hybrid B3LYP and with the range-separated hybrid CAM-B3LYP (CAM) are close to BP, showing that moderate fractions of HF exchange do not strongly alter the results for MPBN. The fact that the CAM data are close to B3LYP and BP indicates that interactions of electrons at large separation and the asymptotic region of the potential do not have a strong effect on the calculated shifts. However, results obtained with BHLYP, a 50% hybrid, are significantly worse. One possible interpretation is that for MPBN, DFT correlation is more important than long-range exchange, and BHLYP has not enough correlation overall, i.e., too much Hartree−Fock. The pNMR shifts obtained for a molecular geometry optimized with the nonhybrid BP functional (ADF calculations) show the same trends regarding the functionals, but the agreement with the experimental data is not as good as for the B3LYP geometry. The sensitivity to structural parameters has previously been explained by the varying degree of delocalization of the spin-density into the phenyl ring depending on the dihedral angle between the phenyl plane and the tBu−NO plane.[5]

Metallocene pNMR chemical shifts have previously been shown to be well reproduced by spin-unrestricted DFT computations with global hybrid functionals.[9] Therefore, these systems represent an excellent test for the present

ZORA HFC implementation as well as an interesting application for the NBO analysis tools. Metallocenes with V, Cr, Mn, Co, and Ni are considered here, with spin multiplicities of 4, 3, 6, 2, and 3, respectively. The experimental ^{13}C chemical shift range is roughly −500 to +1500 ppm, and the proton shifts span a range from about −250 to +300 ppm. An overview of the calculated chemical shifts in comparison with experimental results and with previous calculations is shown in Figure 2 for the PBE0 functional. For a comparison of different functionals, and a comparison with ADF calculations, see the Supporting Information. Experimental metallocene chemical shifts were taken from ref 9, which were converted from a toluene reference to tetramethylsilane. For original reports of the experimental data, see refs 9 and 59−65.

The agreement of the ZORA-DFT calculations with experimental and theoretical reference data is very favorable. Signs and magnitudes of the large (predominantly contact) shifts and the ordering of the metallocenes from largest to smallest shifts are correctly reproduced with the PBE0 functional. The data exhibit some interesting trends that make the metallocenes worthy of a closer examination with the LMO analysis tools. For example, there is a sign change for the carbon shifts when going from triplet Ni (positive carbon shifts) to quartet V. The proton shifts for the Ni complex are negative, and again there is a sign change from Ni to V. Further, the carbon shifts for nickelocene are much larger in magnitude than those for vanadocene, despite the fact that V has three unpaired α-spin-orbitals but Ni has only two.

These two metallocenes (Ni and V), producing the largest positive and the largest negative ^{13}C and proton pNMR shifts, were selected for a detailed analysis. The pNMR chemical shifts in the metallocene series are completely dominated by contact shifts (see Supported Information), which allows us to focus on analyzing the isotropic HFCCs. For aromatic systems, McConnell has shown that proton coupling constants are roughly proportional to the π spin-density on the adjacent carbon and tend to have opposite signs to the carbon HFCCs,[3,66] due to spin-polarization of the C−H σ bonding orbitals. This sign pattern is indeed observed in the metallocene series (note that the manganocene proton shifts are calculated to be slightly negative but measured to be +29 ppm). Since proton shift sign patterns are in most cases coupled to those of the carbons, we limit the LMO analysis to the ^{13}C HFCCs.

It is interesting to note that McConnell and Holm, in 1957 and 1958, discussed the proton shifts in nickelocene, initially in terms of α spin-density being transferred from Ni to the Cp π system[67] and later, reversing the original argument, in terms of backbonding from Cp β−π orbitals into the empty Ni d_π^β orbitals.[68] The analysis discussed below strongly supports the β−π-backbonding mechanism for nickelocene, but it also shows that the α donation mechanism provides a secondary contribution that should not be neglected.

Table 6 lists a summary of the LMO analysis data for the carbon HFCCs in nickelocene and vanadocene. Symmetry labels σ, π, and δ refer to a rotational axis lining up the metal center with the Cp centroids. We focus on nickelocene first. In agreement with previous DFT calculations,[9] for the d^8 Ni^{2+} system, the d_δ and d_σ orbitals are fully occupied (paired), and the formal SOMOs are the two Ni d_π orbitals. The corresponding d_π^α LMOs do not afford large ligand contributions and should therefore be considered as mainly nonbonding. According to the NBO analysis, these LMOs have roughly 2% contributions from Cp carbon p orbitals. The data

Table 6. Localized Molecular Orbital (LMO) Decomposition of the Isotropic ^{13}C Hyperfine Coupling Constant in Nickelocene and Vanadocene in MHz[a]

LMO type	Ni	V
C (core)	0.23	−1.92
σ bonds (NN)	2.40	0.89
other σ bonding/core, same Cp	0.98	−0.64
π bonds, same Cp	0.16	−0.24
other σ bonding/core, other Cp	−0.01	0.02
π bonds, other Cp	0.47	0.03
metal (core)	−0.01	−0.02
metal d_σ	0.02	*0.74
metal d_π	*0.85	
metal d_δ	−0.03	*0.07
$\sum$ analysis	5.06	−1.05
total calcd.	5.06	−1.06

[a]NN = nearest neighbor atoms to the carbon for which the HFCC was calculated. Formal SOMOs indicated by asterisk.

are in line with the high occupations of 0.99 of the corresponding parent NBOs. This finding shows that McConnell's first mechanism, whereby α spin density would be donated from the Ni d_π^α orbitals to unoccupied α orbitals in the Cp rings, contributes to the ^{13}C HFCCs but it is not dominant. Indeed, the LMO analysis for the hyperfine coupling gives direct contributions from the Ni d_π^α LMOs to the ^{13}C coupling constant of 0.85 MHz out of a total of 5.1 MHz. There are large contributions, as expected, from the σ bonding network in the Cp ring, indicating that excess α spin-density in the π system causes a corresponding spin-polarization of the σ orbitals which ultimately creates the large contact shifts. The source of the considerable π spin-density for nickelocene is quickly revealed by the NBO occupations of the formally unoccupied Ni d_π^β orbitals, calculated as 0.40. This means that a significant amount of charge is donated from the Cp π systems to the Ni d_π^β orbitals. The charge donation is visible in several of the β Cp π orbitals exhibiting Ni d_π character (see the Supporting Information for representative isosurface plots of LMOs). The depletion of β spin-density leaves an excess of α spin-density in the Cp rings. The spin-polarization effect on the σ orbitals then unfolds as expected, including spin-polarization of the C−H bonding orbitals leading to the negative proton HFCCs. Thus, the analysis very clearly points to the alternative "back-donation" mechanism suggested by McConnell and Holm[68] as the dominant source of the observed signs of the proton and carbon pNMR shifts in nickelocene. We note in passing that the spin-polarization contributions from the C−H bonding LMOs dominate the proton HFCCs in nickelocene.

In vanadocene, the V^{2+} ion in its formal d^3 configuration affords two unpaired d_δ and one unpaired d_σ orbital, all formally nonbonding. The LMO analysis in Table 6 demonstrates that the contributions from the V d_δ^α orbital to the ^{13}C hyperfine coupling are very small. Relative to the total magnitude of the negative HFCC, the direct contribution from the V d_σ^α orbital is large, and positive. Compared to nickelocene, the NBO analysis gave somewhat larger Cp contributions in the corresponding LMO, 3%, and a lower NBO occupation of 0.97. The larger mixing of V d_σ^α and Cp orbitals is also evident from a comparison of contour plots of the LMOs shown in Figure 3. The difference from Ni might be rationalized by the smaller nuclear charge and corresponding larger spatial extension of the vanadium 3d orbitals. We interpret the situation as follows:
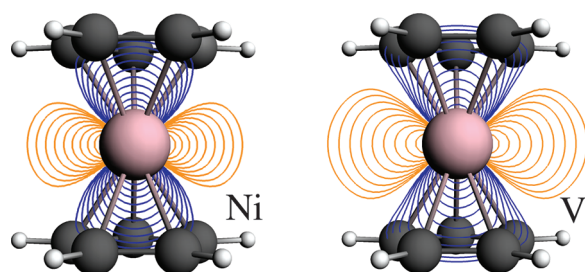
Figure 3. Metal $3d_\sigma^\alpha$ LMOs of nickelocene (left) and vanadocene (right). Contour plot in the *yz* plane, with the Cp centroids aligned along *z*. Contour line values starting at 0.01 au (logarithmic spacing). The orbital in the V complex has a larger spatial extension and larger ligand contributions (see text).

Unlike the Ni case where depletion of π β-spin density, along with some Ni $\rightarrow$ Cp α π donation, leads to spin-polarization of the Cp σ system, which is the main source of the ligand HFC, in vanadocene a small amount of charge donation directly into the Cp σ system gives rise to large positive carbon HFC contributions from the V d_σ and the carbon σ bonds with its nearest neighbors. The NBO output indicates C and H s-orbital (and carbon p_σ) contributions in the V d_σ^α LMO. β-back-donation is present to some degree, as indicated by an occupation of 0.11 of the V d_σ^β NBO which serves to amplify the excess α spin-density originating from the Cp valence σ orbitals centered at the carbon of interest. The charge donation into the Cp σ framework then causes relaxation of the C core orbitals such as to create an excess of β spin density at the C nuclei, with corresponding very large negative contributions to the ^{13}C HFCCs overpowering direct positive Cp valence and V d_σ terms. Additional negative contributions arise from non-nearest neighbor σ orbitals in the Cp ring, and from spin-polarization of the Cp π orbitals. The resulting carbon HFCCs are negative in sign, and much smaller in magnitude than those in nickelocene for two reasons: only one unpaired V d orbital significantly contributes to the spin-density in the Cp rings, compared to two for Ni, and there is a strong cancellation of terms in vanadocene. The C core orbitals provide the largest negative contributions to the ^{13}C HFCCs.

5. SUMMARY AND OUTLOOK

Calculated hyperfine coupling constants (HFCCs) can be analyzed in a chemically intuitive way in terms of localized molecular orbital (LMO) contributions. This allows for new ways to interpret EPR spectra and of the NMR chemical shifts of paramagnetic molecules (pNMR). A new implementation for HFCCs has been carried out in NWChem utilizing the two-component relativistic ZORA Hamiltonian and DFT with nonhybrid functionals, global hybrids, and range-separated hybrids. Spin-orbit (SO) coupling is treated as a perturbation to first order, which gives rise to a linear response PSOSO mechanism in the hyperfine tensor. This mechanism is small relative to the FC+SD expectation value contribution for molecules with light atoms but becomes significant for systems with heavy elements. For NpF$_6$, the PSOSO mechanism dominates the HFCC of Np and contributes roughly 1/4 to 1/3 of the fluorine coupling constant. Benchmark calculations on a test set of radicals with few atoms, covering light and heavy main group elements and metal atoms, show that reasonable agreement with experimental results can be achieved with spin-unrestricted scalar ZORA DFT calculations of HFCCs. Finite-

nucleus effects were modeled with a spherical Gaussian finite nucleus model. For HFCCs of ^{199}Hg, the finite nucleus corrections are up to about 15% relative to the point-nucleus results.

The pNMR chemical shifts for two metallocenes that were analyzed in detail, Ni and V, show that the opposing signs of the chemical shifts and the very different magnitudes are caused by different spin-polarization mechanisms. For nickelocene, the excess α spin-density in the Cp π systems created by α π donation from Ni and, more importantly, β back-donation from Cp to the metal is the main cause of the large positive ^{13}C pNMR shifts. For vanadocene, the LMO analysis points to α spin-density donation from the occupied V d_σ^α orbital to the Cp rings as the main mechanism. The σ interaction causes a relaxation of the carbon 1s shells, which leads to excess β spin-density and concomitant negative carbon HFCCs. The paramagnetic proton shifts are coupled to those of the Cp carbons and exhibit opposite signs, in agreement with the McConnell spin polarization mechanism.[3,66]

■ ASSOCIATED CONTENT

Ⓢ Supporting Information

Additional results for the small-molecule test set, similar to Table 1 but obtained with point nuclei and/or without ZORA scaling. Finite nucleus effects for Hg hyperfine coupling, calculated with nonhybrid functionals. pNMR shifts for metallocenes calculated with different functionals. Isosurface plots of selected nickelocene LMOs. Separate orbital, contact, and PC shieldings for metallocenes calculated with PBE0. This information is available free of charge via the Internet at http://pubs.acs.org

■ AUTHOR INFORMATION

Corresponding Author
*E-mail: jochena@buffalo.edu.

Notes
The authors declare no competing financial interest.

■ ACKNOWLEDGMENTS

■ REFERENCES

(1) Atherton, N. M. *Principles of Electron Spin Resonance*; PTR Prentice Hall: New York, 1993; Ellis Horwood series in physical chemistry Ellis Horwood, pp 46−50, 210.

(2) Eriksson, L. A. ESR Hyperfine Calculations. In *Encyclopedia of Computational Chemistry*; von Ragué Schleyer, P., Ed.; Wiley: Chichester, U.K., 1998; pp 952−958.

(3) Rieger, P. H. *Electron Spin Resonance. Analysis and Interpretation*; The Royal Society of Chemistry: Cambridge, U.K., 2007; pp 3, 27−29.

(4) Bertini, I.; Luchinat, C.; Parigi, G. *Prog. Nucl. Mag. Res. Spectrosc.* **2002**, *40*, 249−273.

(5) Moon, S.; Patchkovskii, S. First-principles calculations of paramagnetic NMR shifts. In *Calculation of NMR and EPR Parameters.*

Theory and Applications; Kaupp, M., Bühl, M., Malkin, V. G., Eds.; Wiley-VCH: Weinheim, Germany, 2004; pp 325−338.

(6) Kaupp, M.; Köhler, F. H. *Coord. Chem. Rev.* **2009**, *253*, 2376−2386.

(7) Rastrelli, F.; Bagno, A. *Chem.—Eur. J.* **2009**, *15*, 7990−8004.

(8) Autschbach, J.; Patchkovskii, S.; Pritchard, B. *J. Chem. Theory Comput.* **2011**, *7*, 2175−2188.

(9) Hrobárik, P.; Reviakine, R.; Arbuznikov, A. V.; Malkina, O. L.; Malkin, V. G.; Köhler, F. H.; Kaupp, M. *J. Chem. Phys.* **2007**, *126*, 024107−19.

(10) Autschbach, J.; Pritchard, B. *Theor. Chem. Acc.* **2011**, *129*, 453−466.

(11) Autschbach, J.; Ziegler, T. *Coord. Chem. Rev.* **2003**, *238/239*, 83−126.

(12) Autschbach, J. Relativistic effects on magnetic resonance parameters and other properties of inorganic molecules and metal complexes. In *Relativistic Methods for Chemists*; Ishikawa, J., Barysz, M., Eds.; Springer UK: London, 2010; Vol. 10, pp 521−598.

(13) van Lenthe, E.; Baerends, E. J.; Snijders, J. G. *J. Chem. Phys.* **1993**, *99*, 4597−4610.

(14) Weinhold, F. Natural bond orbital methods. In *Encyclopedia of Computational Chemistry*; von Ragué Schleyer, P., Ed.; John Wiley & Sons: Chichester, 1998, pages 1792−1811.

(15) Aquino, F.; Govind, N.; Autschbach, J. *J. Chem. Theory Comput.* **2011**, *7*, 3278−3292.

(16) Visscher, L.; Dyall, K. *At. Data Nucl. Data Tables* **1997**, *67*, 207−224.

(17) Autschbach, J. *ChemPhysChem* **2009**, *10*, 2274−2283.

(18) Nichols, P.; Govind, N.; Bylaska, E. J.; de Jong, W. A. *J. Chem. Theory Comput.* **2009**, *5*, 491−499.

(19) Aquino, F.; Govind, N.; Autschbach, J. *J. Chem. Theory Comput.* **2010**, *6*, 2669−2686.

(20) Autschbach, J.; Zheng, S.; Schurko, R. W. *Concepts Magn. Reson. A* **2010**, *36A*, 84−126.

(21) Autschbach, J. *J. Chem. Phys.* **2007**, *127*, 124106−11.

(22) Autschbach, J. *J. Chem. Phys.* **2008**, *128*, 164112−11.

(23) Zheng, S.; Autschbach, J. *Chem.—Eur. J.* **2011**, *17*, 161−173.

(24) Autschbach, J.; Zheng, S. *Magn. Reson. Chem.* **2008**, *46*, S48−S55.

(25) Bohmann, J. A.; Weinhold, F.; Farrar, T. C. *J. Chem. Phys.* **1997**, *104*, 1173−1184.

(26) Boys, S. F. In *Quantum Theory of Atoms, Molecules and the Solid State*; Löwdin, P. O., Ed.; Academic Press: New York, 1966.

(27) Pipek, J.; Mezey, P. G. *J. Chem. Phys.* **1989**, *90*, 4916−4926.

(28) Wolff, S. K.; Ziegler, T.; van Lenthe, E.; Baerends, E. J. *J. Chem. Phys.* **1999**, *110*, 7689−7698.

(29) Bylaska, E. J.; de Jong, W. A.; Govind, N.; Kowalski, K.; Straatsma, T. P.; Valiev, M.; van Dam, J. J.; Wang, D.; Apra, E.; Windus, T. L.; Hammond, J.; Autschbach, J.; Aquino, F.; Nichols, P.; Hirata, S.; Hackler, M. T.; Zhao, Y.; Fan, P.-D.; Harrison, R. J.; Dupuis, M.; Smith, D. M. A.; Glaesemann, K.; Nieplocha, J.; Tipparaju, V.; Krishnan, M.; Vazquez-Mayagoitia, A.; Jensen, L.; Swart, M.; Wu, Q.; Van Voorhis, T.; Auer, A. A.; Nooijen, M.; Crosby, L. D.; Brown, E.; Cisneros, G.; Fann, G. I.; Fruchtl, H.; Garza, J.; Hirao, K.; Kendall, R.; Nichols, J. A.; Tsemekhman, K.; Wolinski, K.; Anchell, J.; Bernholdt, D.; Borowski, P.; Clark, T.; Clerc, D.; Dachsel, H.; Deegan, M.; Dyall, K.; Elwood, D.; Glendening, E.; Gutowski, M.; Hess, A.; Jaffe, J.; Johnson, B.; Ju, J.; Kobayashi, R.; Kutteh, R.; Lin, Z.; Littlefield, R.; Long, X.; Meng, B.; Nakajima, T.; Niu, S.; Pollack, L.; Rosing, M.; Sandrone, G.; Stave, M.; Taylor, H.; Thomas, G.; van Lenthe, J.; Wong, A.; Zhang, Z. *NWChem*, version 6.0 (2011 developer's version); Pacific Northwest National Laboratory: Richland, WA, 2011.

(30) Kendall, R. A.; Aprà, E.; Bernholdt, D. E.; Bylaska, E. J.; Dupuis, M.; Fann, G. I.; Harrison, R. J.; Ju, J.; Nichols, J. A.; Nieplocha, J.; Straatsma, T. P.; Windus, T. L.; Wong, A. T. *Comput. Phys. Commun.* **2000**, *128*, 260−283.

(31) Valiev, M.; Bylaska, E. J.; Govind, N.; Kowalski, K.; Straatsma, T. P.; Dam, H. J. J. V.; Wang, D.; Nieplocha, J.; Apra, E.; Windus, T. L.; de Jong, W. A. *Comput. Phys. Commun.* **2010**, *181*, 1477−1489.

(32) Patchkovskii, S.; Strong, R. T.; Pickard, C. J.; Un, S. *J. Chem. Phys.* **2005**, *122*, 214101−9.

(33) Roos, B. O.; Lindh, R.; Malmqvist, P.; Veryazov, V.; Widmark, P. *J. Phys. Chem. A* **2005**, *109*, 6575−6579.

(34) Jensen, F. *J. Chem. Theory Comput.* **2006**, *2*, 1360−1369.

(35) Jensen, F. *Theor. Chem. Acc.* **2009**, *126*, 371−382.

(36) Baerends, E. J.; Ziegler, T.; Autschbach, J.; Bashford, D.; Bérces, A.; Bickelhaupt, F. M.; Bo, C.; Boerrigter, P. M.; Cavallo, L.; Chong, D. P.; Deng, L.; Dickson, R. M.; Ellis, D. E.; van Faassen, M.; Fan, L.; Fischer, T. H.; Fonseca Guerra, C.; Ghysels, A.; Giammona, A.; van Gisbergen, S. J. A.; Götz, A. W.; Groeneveld, J. A.; Gritsenko, O. V.; Grüning, M.; Gusarov, S.; Harris, F. E.; van den Hoek, P.; Jacob, C. R.; Jacobsen, H.; Jensen, L.; Kaminski, J. W.; van Kessel, G.; Kootstra, F.; Kovalenko, A.; Krykunov, M. V.; van Lenthe, E.; McCormack, D. A.; Michalak, A.; Mitoraj, M.; Neugebauer, J.; Nicu, V. P.; Noodleman, L.; Osinga, V. P.; Patchkovskii, S.; Philipsen, P. H. T.; Post, D.; Pye, C. C.; Ravenek, W.; Rodríguez, J. I.; Ros, P.; Schipper, P. R. T.; Schreckenbach, G.; Seldenthuis, J. S.; Seth, M.; Snijders, J. G.; Solà, M.; Swart, M.; Swerhone, D.; te Velde, G.; Vernooijs, P.; Versluis, L.; Visscher, L.; Visser, O.; Wang, F.; Wesolowski, T. A.; van Wezenbeek, E. M.; Wiesenekker, G.; Wolff, S. K.; Woo, T. K.; Yakovlev, A. L. *Amsterdam Density Functional*; Vrije Universiteit: Amsterdam, The Netherlands. http://www.scm.com (accessed 01/02/2012).

(37) van Lenthe, E.; Baerends, E. J. *J. Comput. Chem.* **2003**, *24*, 1142−1156.

(38) Nakajima, T.; Hirao, J. *J. Chem. Phys.* **2002**, *116*, 8270−8275.

(39) Tsuchiya, T.; Abe, M.; Nakajima, T.; Hirao, K. *J. Chem. Phys.* **2001**, *115*, 4463−4472.

(40) Malkin, E.; Malkin, I.; Malkina, O. L.; Malkin, V. G.; Kaupp, M. *Phys. Chem. Chem. Phys.* **2006**, *8*, 4079−4085.

(41) Kutzelnigg, W.; Fleischer, U.; Schindler, M. The IGLO-Method: Ab Initio Calculation and Interpretation of NMR Chemical Shifts and Magnetic Susceptibilities. In *NMR Basic Principles and Progress*; Diehl, P., Fluck, E., Gunther, H., Kosfeld, R., Seelig, J., Eds.; Springer-Verlag: Heidelberg, Germany, 1990; Vol. 23, pp 165−262.

(42) Glendening, E. D.; Badenhoop, J. K.; Reed, A. E.; Carpenter, J. E.; Bohmann, J. A.; Morales, C. M.; Weinhold, F. NBO 5.0; University of Wisconsin: Madison, WI, 2001. http://www.chem.wisc.edu/~nbo5 (accessed 01/02/2012).

(43) Becke, A. D. *Phys. Rev. A* **1988**, *38*, 3098−3100.

(44) Perdew, J. P. *Phys. Rev. B* **1986**, *33*, 8822−8824.

(45) Becke, A. D. *J. Chem. Phys.* **1993**, *98*, 5648−5652.

(46) Becke, A. D. *J. Chem. Phys.* **1993**, *98*, 1372−1377.

(47) Yanai, T.; Tew, D. P.; Handy, N. C. *Chem. Phys. Lett.* **2004**, *393*, 51−57.

(48) Weltner, W., Jr. *Magnetic Atom and Molecules*; Van Nostrand Reinhold: New York, 1983; p 379.

(49) Holmberg, R. W. *J. Chem. Phys.* **1969**, *51*, 3255−3260.

(50) Van Zee, R. J.; Ferrante, R. F.; Weltner, W. Jr. *J. Chem. Phys.* **1985**, *83*, 6181−6187.

(51) Knight, L. B. Jr.; Weltner, W. Jr. *J. Chem. Phys.* **1971**, *55*, 2061−2070.

(52) Knight, L. B. Jr.; Fisher, T. A.; Wise, M. B. *J. Chem. Phys.* **1981**, *74*, 6009−6013.

(53) De Vore, T. C.; Weltner, W. *J. Am. Chem. Soc.* **1977**, *99*, 4700−4703.

(54) Butler, J. E.; Hutchison, C. A. Jr. *J. Chem. Phys.* **1981**, *74*, 3102−3119.

(55) Case, D. A. *J. Chem. Phys.* **1985**, *83*, 5792−5796.

(56) Pyykkö, P. *Chem. Phys.* **1977**, *22*, 289−296.

(57) Lipas, P. O.; Pyykkö, P.; Pajanne, E. *J. Chem. Phys.* **1973**, *58*, 3248−3254.

(58) Autschbach, J. *Theor. Chem. Acc.* **2004**, *112*, 52−57.

(59) Eicher, H.; Köhler, F. H. *Chem. Phys.* **1988**, *128*, 297−309.

(60) Hebendanz, N.; Köhler, F. H.; Müeller, G.; Riede, J. *J. Am. Chem. Soc.* **1986**, *108*, 3281−3289.

(61) Hebendanz, N.; Köhler, F. H.; Scherbaum, F.; Schlesinger, B. *Magn. Reson. Chem.* **1989**, *27*, 798−802.

(62) Köhler, F. H.; Prössdorf, W. *J. Am. Chem. Soc.* **1978**, *100*, 5970−5972.

(63) Köhler, F. H.; Xie, X. *Magn. Reson. Chem.* **1997**, *35*, 487−492.

(64) Rettig, M. F.; Drago, R. S. *J. Am. Chem. Soc.* **1969**, *91*, 1361−1370.

(65) Rettig, M. F.; Drago, R. S. *Chem. Commun. (London)* **1966**, 891−892.

(66) McConnell, H. M. *J. Chem. Phys.* **1956**, *24*, 764.

(67) McConnell, H. M.; Holm, C. H. *J. Chem. Phys.* **1957**, *27*, 314.

(68) McConnell, H. M.; Holm, C. H. *J. Chem. Phys.* **1958**, *28*, 749.

(69) Malkin, E.; Repisky, M.; Komorovsky, S.; Mach, P.; Malkina, O. L.; Malkin, V. G. *J. Chem. Phys.* **2011**, *134*, 044111.